

A Novel Method to Mitigate Real-Imaginary Image Imbalance in Microwave Tomography

Md Asiful Islam, Asimina Kiourti, *Member, IEEE* and John L. Volakis, *Fellow, IEEE*

Abstract—Typical microwave tomographic techniques reconstruct the real part of the permittivity with much greater accuracy as compared to the imaginary part. In this paper, we propose a method to mitigate the imbalance between the reconstructed complex permittivity components and increase the accuracy of the overall image recovery. To do so, the complex permittivity in the imaging domain is expressed as a weighted sum of a few preselected permittivities, close to the range of the expected values. To obtain the permittivity weights, a Gauss-Newton algorithm is employed. Image reconstructions from simulated and experimental data for different biomedical phantoms are presented. Results show that the proposed method leads to excellent reconstruction with balanced real and imaginary parts, across different scenarios.

Index Terms—Complex permittivity, Gauss-Newton algorithm, inverse problems, microwave tomographic imaging.

I. INTRODUCTION

MICROWAVE Tomographic Imaging (MTI) is a potential imaging modality for a variety of applications, such as non-destructive industrial monitoring [1], structural imaging [2], breast cancer diagnosis [3] and other biomedical applications [4]-[7]. Depending on the application, MTI can be an alternative or complementary option to popular imaging modalities such as X-ray Computed Tomography (X-ray CT), Magnetic Resonance Imaging (MRI), optical tomography, electrical capacitance tomography (ECT), etc.

In MTI, the imaging domain is surrounded by an array of antennas that transmit low power microwave signal. Typically, only one antenna is excited at a time while the others act as receivers to measure the scattered signals. This process is repeated for all the antennas to construct a data vector for image reconstruction. The later entails the prediction of the dielectric properties across the imaging domain. This estimation of dielectric properties is carried out on a discrete mesh, composed of electrically small elements [8]-[12]. To start the iterative image reconstruction process, an initial dielectric permittivity distribution of the imaging domain is

assumed [8]-[14]. But if the actual permittivity distribution is significantly different from the assumed initial reference, nonlinear iterative algorithms should be used [14]-[17]. For example, in [16] a nonlinear image reconstruction method for breast cancer detection was proposed combining the Gauss-Newton and Conjugate Gradient Least Square (CGLS) methods. Of course, MTI image reconstruction is more easily carried out [4] when the permittivity distribution is not significantly different from the reference distribution (differential imaging). As an example to this, the MTI method was successfully used to recover the permittivity during an interstitial thermal therapy in a human head [5]. MTI was also employed in [6] to reconstruct a weak scatterer representing a microwave absorber. In [8], MTI was used to carry out real-time monitoring of dielectric contrast materials in an otherwise homogeneous domain. A subspace-based variational Born iterative method for differential microwave imaging is reported in [9]. However, all these MTI-based methods can reliably reconstruct the real part of the permittivity, but not the imaginary part. Of course, the latter is a key parameter for biological media. The real and imaginary part convey different information depending on the application. For example, in industrial flow imaging, the relative permittivity distribution is related to the flow pattern, whereas the conductivity distribution may convey information about the impurity in the domain [18]. Alternatively, in biomedical applications, the real part of the permittivity is more related to the bound water content [19]. Bound water may be a potential indicator of pathological conditions like cancer, edema etc. [19]. On the other hand, conductivity (imaginary part of the permittivity) distribution in a biological domain may be used for noninvasive temperature sensing for therapeutic applications [4].

Based on past experience [7]-[8] and extensive literature search, we conclude that the accuracy in extracting relative permittivity (real part) of the imaging domain outperforms that of conductivity (imaginary part) [16]-[17], [20]-[22]. But, very few attempts have been made to address this issue. As an example, in [17], a pre-scaling approach is employed. However, the robustness of this approach is not clear. To maximize the information obtained from microwave tomographic imaging, it is essential to develop an algorithm capable of producing images of both the relative permittivity and conductivity with similar accuracy.

As a remedy to the imbalanced reconstruction of relative permittivity and conductivity, in this paper, a new approach is presented. Our approach uses fraction parameters instead of the complex permittivity directly. These fraction parameters

Manuscript received Jan 09, 2019, revised May 20, 2019, accepted Aug 12, 2019.

M. A. Islam is with the Electrical and Electronic Engineering Department, Bangladesh University of Engineering and Technology, Dhaka 1205, Bangladesh, A. Kiourti is with the ElectroScience Laboratory, Electrical and Computer Engineering Department, The Ohio State University, Columbus, OH 43212, USA, J. L. Volakis is with the College of Engineering and Computing, Florida International University, Miami, FL 33174, USA. (e-mails: maislam@eee.buet.ac.bd, kiourti.1@osu.edu, jvolakis@fiu.edu).

represent the weights of the preselected permittivities to reconstruct the imaging domain. Notably, use of the fraction parameters has been done previously for other applications [24]-[25]. Unlike those works, our goal of fraction imaging is to mitigate the imbalance between real and imaginary portion of the complex permittivity. To do so, we developed an iterative algorithm based on the Gauss-Newton (GN) method to calculate the fraction parameters. Both the relative permittivity and conductivity images are then obtained from the fraction parameters once they are available. It is shown that our method overcomes the imbalance between the relative permittivity and the conductivity. Preliminary results for 2D cases were already presented by the authors [26]. In this paper, we present the details of the method and present images employing both synthesized (simulated) and experimental data using biomedical phantoms. Specifically, numerous imaging scenarios for small to moderate permittivities found in reference distributions are investigated and reconstructed. Overall, the proposed method has the potential to mitigate the long-standing permittivity/conductivity image imbalance for microwave tomography. As this issue mostly affects cases where the imaging medium is lossy, our analysis focuses only on MTI applications for biological media.

II. COMPLEX PERMITTIVITY RECONSTRUCTION METHOD

A. Permittivity Representation Using Fraction Parameters

An example domain to be imaged is shown in Fig. 1. From the set of dipole transceivers placed around the domain, one antenna is excited at a time while the others are used as receivers. This process is repeated until all antennas are excited one-by-one. Scattering parameters are collected from all receiver antennas and stacked in one vector, $\{\mathbf{S}\}_{meas}$ to form the $M \times 1$ measurement vector, M being the number of measurements.

We define the complex relative permittivity of the domain of interest (DOI) shown in Fig. 1 as

$$\{\boldsymbol{\varepsilon}\} = \{\varepsilon_n; n = 1, 2, 3, \dots, N_E\} \quad (1)$$

In this, N_E refers to the total number of pixels subdividing the DOI. A key aspect of the fraction method is to express the permittivity of the n -th pixel as

$$\varepsilon_n = \sum_{t=1}^{N_{dielec}} r_{t,n} e_t \quad (2)$$

In this, $r_{1,n}, r_{2,n}, \dots, r_{N_{dielec},n}$ represent the permittivity fractions selected *a priori* to synthesize the pixel's permittivity, ε_n . That is, ε_n is a weighted linear sum of the preselected permittivities $e_1, e_2, \dots, e_{N_{dielec}}$ where N_{dielec} = no. of preselected permittivities. Obviously, as r 's are fractions

$$\sum_{t=1}^{N_{dielec}} r_{t,n} = 1$$

with, $0 \leq r_{t,n} \leq 1$ (3)

We remark that the permittivity values $e_1, e_2, \dots, e_{N_{dielec}}$ are selected *a priori* and the inverse problem involves the finding of the unknown fractions $r_{1,n}, r_{2,n}, \dots, r_{N_{dielec},n}$ for each pixel. Notably, this kind of *a priori* information is typically available (or at least can be estimated) for practical biomedical domains.

B. Reconstruction of Fraction Parameters

In conventional microwave imaging methods, the goal is to find $\{\boldsymbol{\varepsilon}\}$ using the measured scattering data, $\{\mathbf{S}\}_{meas}$. To do so, one proceeds to solve the following optimization problem [8]

$$C(\{\boldsymbol{\varepsilon}\}) = \underset{\{\boldsymbol{\varepsilon}\}}{\operatorname{argmin}} \frac{1}{2} (\|\{\mathbf{S}\}_{meas} - F(\{\boldsymbol{\varepsilon}\})\|^2 + \mu \| [R] (\{\boldsymbol{\varepsilon}\} - \{\boldsymbol{\varepsilon}^0\}) \|^2) \quad (4)$$

where $\{\mathbf{S}\}_{meas}$ is the measurement vector and $F(\{\boldsymbol{\varepsilon}\})$ is the forward problem solution for a set of given $\{\boldsymbol{\varepsilon}\}$. That is, $F(\{\boldsymbol{\varepsilon}\}) = \{\mathbf{S}\}_{calc}$ for the given $\{\boldsymbol{\varepsilon}\}$ and $\|\cdot\|$ is the L_2 norm of a vector. The second term in (4) is referred to as the regularization functional with $[R]$ denoting an appropriate regularization matrix, μ is a chosen scalar controlling the level of regularization (user specified) and $\{\boldsymbol{\varepsilon}^0\}$ is any assumed initial permittivity distribution.

Instead of solving for the desired $\{\boldsymbol{\varepsilon}\}$, in this paper, we propose to only solve for the fraction parameters. To do so, the optimization process is revised as follows

$$C(\{\tilde{\mathbf{r}}\}) = \underset{\{\tilde{\mathbf{r}}\}}{\operatorname{argmin}} \frac{1}{2} (\|\{\mathbf{S}\}_{meas} - F(\{\tilde{\mathbf{r}}\})\|^2 + \mu \| [R] (\{\tilde{\mathbf{r}}\} - \{\tilde{\mathbf{r}}^0\}) \|^2) \quad (5)$$

$$\text{with, } \{\tilde{\mathbf{r}}\} = \{\tilde{\mathbf{r}}\}_t \quad (6)$$

From (3), $\{\tilde{\mathbf{r}}\}_t$ represents an $N_E \times 1$ vector of the fraction parameters for all the pixel elements in the DOI. For the sake of avoiding repetition, the subscript ' t ' will be omitted hereafter. As was the case of $\{\boldsymbol{\varepsilon}^0\}$, $\{\tilde{\mathbf{r}}^0\}$ is any assumed initial value (typically set to the same real number for all the pixels) of the fraction parameters.

The optimization problem in (5) can be solved via the conventional Gauss-Newton method. As reported in [8], a fast implementation of the Gauss-Newton method can be carried out, avoiding the forward solution in each iteration, by introducing the Taylor series expansion

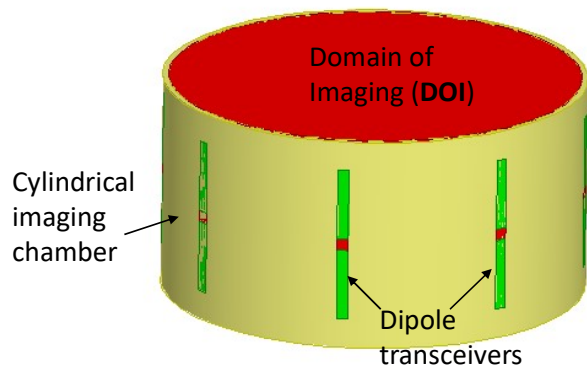


Fig. 1. Geometrical configuration of the imaging domain.

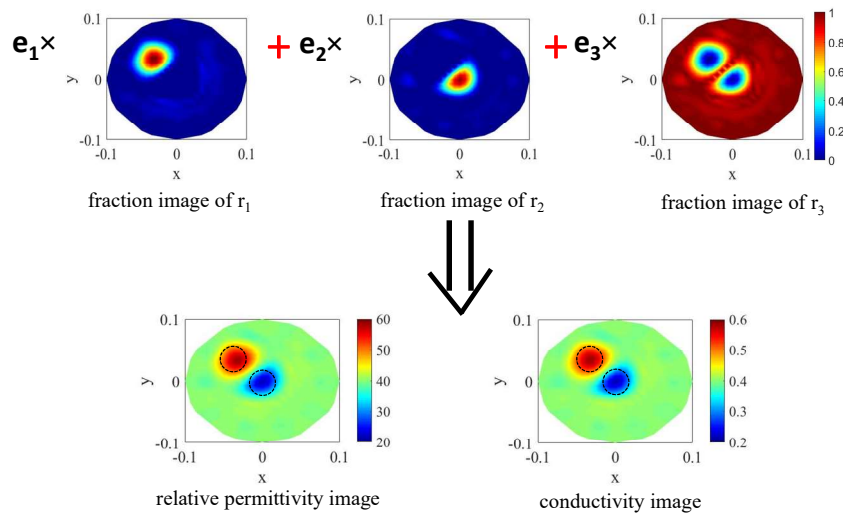


Fig. 2. Image reconstruction process when three fraction parameters ($N_{dielec} = 3$) are used. The x and y axes are in meters.

$$F(\{\tilde{\mathbf{r}}^k\}) \approx F(\{\tilde{\mathbf{r}}^0\}) + [J_{\tilde{\mathbf{r}}}] (\{\tilde{\mathbf{r}}^k\} - \{\tilde{\mathbf{r}}^0\}) \quad (7)$$

Here, $[J_{\tilde{\mathbf{r}}}]$ is the $M \times N_E$ Jacobian matrix with the superscript ' k ' denoting the k -th iteration. MTI using the proposed method in fully nonlinear inverse scattering [16] will be pursued in some future work. It is noted that, unlike typical microwave imaging where the Jacobian matrix is calculated with respect to the permittivities [4]-[6], [8], [16]-[17], here we calculate the Jacobian matrix with respect to the fraction parameters. Specifically, an element of the Jacobian matrix is given by

$$J_{r_t, mn} = \frac{\partial F_m}{\partial \varepsilon_n} \frac{\partial \varepsilon_n}{\partial r_{t,n}} \quad (8)$$

and, from (2)

$$J_{r_t, mn} = \frac{\partial F_m}{\partial \varepsilon_n} e_t = J_{\varepsilon} e_t \quad (9)$$

In this, ' m ' refers to the m -th measurement point among the total M number of measurements, ' n ' is the n -th pixel and ' t ' is the t -th preselected permittivity used in (2) to calculate the pixel's actual permittivity. In (9), e_t is a constant and J_{ε} is calculated using the adjoint method [16].

By using the Gauss-Newton iterative method to solve (5), we get,

$$\begin{aligned} \{\mathbf{r}_1^{k+1}\} &= \{\mathbf{r}_1^k\} - \alpha (B_1^k)^{-1} G_1^k \\ \{\mathbf{r}_2^{k+1}\} &= \{\mathbf{r}_2^k\} - \alpha (B_2^k)^{-1} G_2^k \\ &\vdots \\ &\vdots \end{aligned}$$

$$\{\mathbf{r}_{N_{dielec}}^{k+1}\} = 1 - (\{\mathbf{r}_1^{k+1}\} + \{\mathbf{r}_2^{k+1}\} \dots + \{\mathbf{r}_{N_{dielec}-1}^{k+1}\}) \quad (10)$$

In the above, $[G_t^k]$ and $[B_t^k]$ are the gradient and Hessian matrices calculated from (5) with respect to r_t at the k -th iteration and α is the step size [27]. Notably, the last equation of (10) is due to the condition (3). Another important condition enforced at each iteration is (3). This condition ensures the

stability of the iterative algorithm. Notably, conventional algorithms used to reconstruct the permittivity do not typically employ such bound check.

In (10), $[G_t^k]$ and $[B_t^k]$ are calculated from (5) as follows

$$[G_t^k] = [J_{r_t}]^T (\{\mathbf{S}\}_{meas} - F(\{\mathbf{r}_t^k\})) + \mu [R^T R] (\{\mathbf{r}_t^k\} - \{\mathbf{r}_t^0\}) \quad (11)$$

$$[B_t^k] = [J_{r_t}^T J_{r_t}] + \mu [R^T R] \quad (12)$$

Here, $[J_{r_t}]_{N_E \times M}^T$ is the transpose of the Jacobian matrix for the known permittivity and $[R^T R] = [I]$, where $[I]$ is an identity matrix. Notably, different kinds of regularization matrices can be employed [27], depending on the application. To solve for $\{\tilde{\mathbf{r}}\}$, (10) is iterated until convergence is achieved. The resulting fraction parameters $\{\mathbf{r}_t\}$ are then used to obtain the complex permittivity across the DOI. The process of obtaining relative permittivity and conductivity from the reconstructed fraction parameters is explained in Fig. 2. For this example, we used a set of three ($N_{dielec} = 3$) known permittivities in the DOI. We set $e_1 = 60 - j8.7$ (conductivity=0.6 S/m), $e_2 = 20 - j2.88$ (conductivity=0.2 S/m) and $e_3 = 40 - j5.75$ (conductivity=0.4 S/m). Hence, (5) needs to be solved for the unknown fraction parameters $\{\tilde{\mathbf{r}}\}_1$, $\{\tilde{\mathbf{r}}\}_2$ and $\{\tilde{\mathbf{r}}\}_3$. Once $\{\tilde{\mathbf{r}}\}_1$, $\{\tilde{\mathbf{r}}\}_2$ and $\{\tilde{\mathbf{r}}\}_3$ are reconstructed, as shown in Fig. 2, they can be used to obtain the complex permittivity across the DOI from

$$e_1 \{\tilde{\mathbf{r}}\}_1 + e_2 \{\tilde{\mathbf{r}}\}_2 + e_3 \{\tilde{\mathbf{r}}\}_3 = \{\tilde{\mathbf{E}}\}_{re} - j \{\tilde{\mathbf{E}}\}_{im}$$

In the above, $\{\tilde{\mathbf{E}}\}_{re}$, $\{\tilde{\mathbf{E}}\}_{im}$ are $N_E \times I$ vectors of the real and imaginary parts of the complex permittivity, respectively, for each pixel. In Fig. 2, all the $N_E \times I$ vectors $\{\tilde{\mathbf{r}}\}_1$, $\{\tilde{\mathbf{r}}\}_2$, $\{\tilde{\mathbf{r}}\}_3$ and $\{\tilde{\mathbf{E}}\}_{re}$, $\{\tilde{\mathbf{E}}\}_{im}$ are plotted as 2D images to better explain the concept.

We remark here that the accuracy of reconstruction for both the relative permittivity and conductivity parts of the complex

permittivity is excellent (quantitatively assessed using (14) later). We believe that this improved accuracy is due to two key reasons: 1) use of the preselected permittivities to better predict the domain's permittivity (notably, if any one of the preselected permittivity elements is non-existing in the actual imaging domain, the fraction parameter of that element will be zero), and 2) significant reduction of the search space for finding the fraction parameters, r , implying a more robust solution.

III. IMAGING RESULTS USING SYNTHETIC DATA

For validation, we present several imaging scenarios employing biological phantoms. As is well-known, biological media are substantially lossy at microwave frequencies and hence, the issue of image imbalance between the relative permittivity and conductivity parts of the complex permittivity can be more pronounced. Hence, the proposed method to mitigate this imbalance would be particularly beneficial for biomedical applications.

A. Simulation Set-up

The simulation set-up was shown in Fig. 1. This is a glass cylinder with relative permittivity, $\epsilon_r=2.4$, diameter=20cm and height=10cm. As transceivers, we chose a set of 8 dipole antennas placed around the cylinder on the outer surface as shown in Fig. 1. If possible, the transceiver antennas could be placed on the inside surface of the glass cylinder to minimize mismatches. However, for our initial testing, we chose to place them on the outer surface. We used a suitable operating frequency to ensure reasonable spatial resolution and sufficient penetration into the imaging domain. All dipoles were identical and terminated by 50 Ω matched load. We set the background and anomaly relative permittivity so that the values represent typical biological media as obtained from [29]-[30].

As already mentioned in Section II, data measurements are carried out by exciting one antenna at a time while all others are receiving. For collecting synthetic data, Ansys HFSS full-wave simulation is carried out. It should be noted, however, that unlike most other microwave imaging approaches [13]-[16], we use a full wave forward solver taking into account all the antennas. Hence, all wave phenomena and inter-antenna couplings are accounted for. This, in turn, yields more accurate solution for the forward problem to reduce the so called *model error* [16]. Using the scattering matrix obtained from the simulation, we get the necessary transmission coefficients, S_{qm} , where 'q' and 'm' refer to two different antennas, for every possible pair of antennas. The scattering matrix takes the following form [7],

$$[S]_{scat} = \begin{bmatrix} S_{11} & \cdots & S_{1Q} \\ \vdots & \ddots & \vdots \\ S_{Q1} & \cdots & S_{QQ} \end{bmatrix} \quad (13)$$

In (13), only the upper or lower triangular elements of $[S]_{scat}$ provide unique transmission coefficients (as the medium is reciprocal). We collected two sets of data, with and

without the anomalies present in the DOI, and obtained the two scattering matrices, $[S]_{tot}$ and $[S]_{inc}$, respectively. Then the elements of the $S_{qm,scat}$ matrix were calculated from, $S_{qm,scat} = S_{qm,tot} - S_{qm,inc}$. The lower/upper triangular elements of $[S]_{scat}$, were employed in (10) to solve the imaging problem.

B. Imaging Results

Now, to demonstrate the efficacy and robustness of the method, we will show imaging results using the proposed fraction based imaging method for several different scenarios.

Case-1:

Firstly, we consider an imaging domain with three anomalies, each being a 2.25 cm diameter cylinder with relative permittivity $\epsilon_{r,anom} = 60 - j\frac{0.6}{w\epsilon_0}$ and placed in the background of $\epsilon_{r,b} = 40 - j\frac{0.4}{w\epsilon_0}$. For image reconstruction, we have utilized $N_{dielrec} = 2$ with *a priori* info $e_1=40 - j\frac{0.4}{w\epsilon_0}$, $e_2=60 - j\frac{0.6}{w\epsilon_0}$.

As is well known, actual data can be potentially corrupted by measurement noise and also *model error* [28]. Combinedly, we refer to them as 'measurement error'. Hence, to assess the performance of the proposed imaging algorithm in the presence of measurement error, we perform an analysis of the dependence of the same in the presence of additive Gaussian white noise with different signal-to-noise ratio (SNR) as shown in Fig. 3. The reconstructed image quality severely degrades for SNR=10dB, as shown in Fig. 3(d). On the other hand, the image quality is acceptable for SNR=20dB as shown in Fig. 3(b). Hence, we will use this SNR in the following part of this paper while showing image reconstruction employing synthetic data.

Now, to compare the efficacy of the proposed method with that of a standard MTI method, image reconstruction has been shown in Figs. 4(a)-(b) using 'direct' method ('direct' means minimizing the cost function of Eq. (4) as opposed to (5)) and in Fig. 4(c)-(d) using proposed fraction imaging method. Again, we employed the modified Gauss-Newton algorithm, previously reported by the authors [8], to solve the 'direct' imaging problem. As seen from Figs. 4(a)-(b), the image reconstruction accuracy using 'direct' method is different for the relative permittivity and conductivity (see Table I). By contrast, the accuracy of the relative permittivity and conductivity is balanced while using the proposed method (see Table I). The fact that the relative permittivity is better reconstructed than the conductivity has been reported in the past [16]-[17], [20]-[22]. Here, it is shown that the proposed method drastically improves the accuracy of the conductivity reconstruction as shown in Figs. 4(c)-(d). Also, the overall image quality is better with our proposed method.

The accuracies of the reconstructions for different imaging scenarios including that in Fig. 4 are quantitatively assessed using an error metric [31]

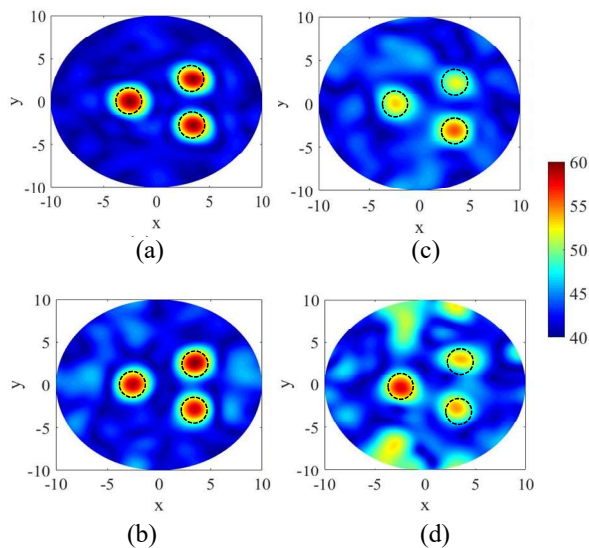


Fig. 3. Reconstructed relative permittivity images in presence of three anomalies using proposed algorithm employing (a) SNR=60 dB, (b) SNR=20 dB, (c) SNR=15 dB, (d) SNR=10dB. The x and y axes are in centimeters.

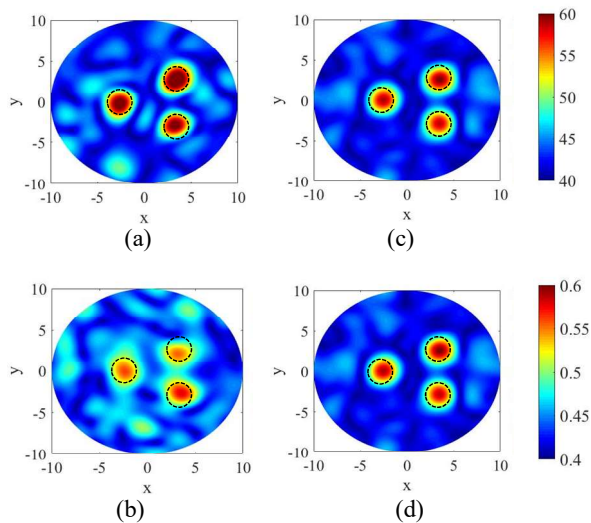


Fig. 4. Reconstructed images in presence of three anomalies using simulation data (SNR 20dB) for Case-1: (a) relative permittivity (direct), (b) conductivity (direct), (c) relative permittivity (fraction method), (d) conductivity (fraction method). The dashed circular lines indicate the actual position of the anomaly. The x and y axes are in centimeters.

$$error = \frac{\sum_{k=1}^{NE} |\varepsilon_{k, reconstructed} - \varepsilon_{k, exact}|}{\sum_{k=1}^{NE} |\varepsilon_{k, exact}|} \quad (14)$$

where $\varepsilon_{k, reconstructed}$ refers to the reconstructed relative permittivity/conductivity and $\varepsilon_{k, exact}$ refers to the exact permittivity/conductivity of the k -th pixel. Table I shows $error$ values from (14) for the images shown in Figs. 4-8.

Case-2:

Next, we consider a more complex scenario where we have, as shown in Fig. 5, two relative permittivity anomalies and one conductivity anomaly in the imaging domain. Though this type of scenario (where relative permittivity and conductivity anomalies have different locations) is not encountered in practice, we present it here to demonstrate the capabilities of

the proposed algorithm. Also, the two anomalies have different relative permittivity as opposed to Case-1 where all the anomalies have the same permittivity. For image reconstruction, we have utilized $N_{dielec} = 3$ with *a priori* info $\varepsilon_1 = 40 - j \frac{0.4}{\omega \varepsilon_0}$, $\varepsilon_2 = 50 - j \frac{0.48}{\omega \varepsilon_0}$ and $\varepsilon_3 = 60 - j \frac{0.4}{\omega \varepsilon_0}$. Successful image reconstruction (see *error* in Table I) is shown in Fig. 5 where 3 fraction parameter images are shown at the top (Fig. 5(a)) and corresponding relative permittivity (Fig. 5(b)) and conductivity (Fig. 5(c)) at the bottom. Overall, the image quality was good with minor artifacts present. Notably, in this case, the *a priori* info chosen are identical to the actual permittivities present in the domain. Table II summarizes all the imaging cases with the dielectrics present in the imaging domain along with the *a priori* info employed in the reconstruction process.

Case-3:

To further assess the performance of the algorithm, in this example, we increased the number of anomalies from 3 to 5 (see Table II). Also, the chosen *a priori* permittivities are the same as those actually present in the domain. The imaging domain is similar to a typical breast cancer imaging scenario where the breast is immersed in a matching liquid. This is evident from the actual permittivity plot (in Fig. 6) where the deep blue region along the circular periphery represents matching liquid and inside of it, there exists permittivity typically found in breasts. The maroon circular region found inside the yellow rectangular region represents a tumor. Fig. 6(a) shows the 5 fraction parameter images and Fig. 6(b)-(c) presents the corresponding reconstructed images of both relative permittivity and conductivity. From Fig. 6(a), we see that the highest *a priori* permittivity takes part in the reconstruction the most. Also, Fig. 6(b)-(c) show that though the reconstructed values are lower than the actual ones, the high relative permittivity/conductivity tumor can be clearly identified in the reconstructed images. Again, the accuracy of both the relative permittivity and conductivity images are similar (see Table I).

Case-4:

The imaging domain in this case is the same to the one used in case-3. The only exception is that we employed 3 *a priori* permittivities (instead of 5) for the image reconstruction as listed in Table II. The goal is to show the efficacy of the

TABLE I
RECONSTRUCTION ERROR FROM (14) FOR DIFFERENT IMAGING SCENARIOS

Image	$error$ (relative permittivity)	$error$ (conductivity)
Fig. 4	0.183 (direct), 0.088 (proposed)	0.247 (direct), 0.088 (proposed)
Fig. 5	0.091	0.110
Fig. 6	0.338	0.343
Fig. 7	0.318	0.325
Fig. 8	0.258	0.267
Fig. 11	0.195 (Fig. 11(a)), 0.105 ((Fig. 11(b))), 0.098 ((Fig. 11(c)))	0.256 (Fig. 11(a)), 0.105 ((Fig. 11(b))), 0.098 ((Fig. 11(c)))

TABLE II
DIFFERENT IMAGING SCENARIOS AND USE OF *A PRIORI* INFO

Image	Dielectrics Present in Imaging Domain	<i>A Priori</i> Permittivities Employed	Comment
Case-1 (Fig. 4(c)-(d))	$\epsilon_1 = 40 - j\frac{0.4}{w\epsilon_0}$ $\epsilon_2 = 60 - j\frac{0.6}{w\epsilon_0}$	$e_1 = 40 - j\frac{0.4}{w\epsilon_0}$ $e_2 = 60 - j\frac{0.6}{w\epsilon_0}$	Same actual and <i>a priori</i> permittivities
Case-2 (Fig. 5)	$\epsilon_1 = 40 - j\frac{0.4}{w\epsilon_0}$ $\epsilon_2 = 50 - j\frac{0.48}{w\epsilon_0}$ $\epsilon_3 = 60 - j\frac{0.4}{w\epsilon_0}$	$e_1 = 40 - j\frac{0.4}{w\epsilon_0}$ $e_2 = 50 - j\frac{0.48}{w\epsilon_0}$ $e_3 = 60 - j\frac{0.4}{w\epsilon_0}$	Same actual and <i>a priori</i> permittivities
Case-3 (Fig. 6)	$\epsilon_1 = 10 - j\frac{0.83}{w\epsilon_0}$ $\epsilon_2 = 12 - j\frac{1.0}{w\epsilon_0}$ $\epsilon_3 = 24 - j\frac{2.0}{w\epsilon_0}$ $\epsilon_4 = 35 - j\frac{3.0}{w\epsilon_0}$ $\epsilon_5 = 5 - j\frac{0.41}{w\epsilon_0}$	$e_1 = 10 - j\frac{0.83}{w\epsilon_0}$ $e_2 = 12 - j\frac{1.0}{w\epsilon_0}$ $e_3 = 24 - j\frac{2.0}{w\epsilon_0}$ $e_4 = 35 - j\frac{3.0}{w\epsilon_0}$ $e_5 = 5 - j\frac{0.41}{w\epsilon_0}$	Same actual and <i>a priori</i> permittivities
Case-4 (Fig. 7)	$\epsilon_1 = 10 - j\frac{0.83}{w\epsilon_0}$ $\epsilon_2 = 12 - j\frac{1.0}{w\epsilon_0}$ $\epsilon_3 = 24 - j\frac{2.0}{w\epsilon_0}$ $\epsilon_4 = 35 - j\frac{3.0}{w\epsilon_0}$ $\epsilon_5 = 5 - j\frac{0.41}{w\epsilon_0}$	$e_1 = 10 - j\frac{0.83}{w\epsilon_0}$ $e_2 = 35 - j\frac{3.0}{w\epsilon_0}$ $e_3 = 5 - j\frac{0.41}{w\epsilon_0}$	Actual and <i>a priori</i> permittivities are different
Case-5 (Fig. 8)	$\epsilon_1 = 10 - j\frac{0.83}{w\epsilon_0}$ $\epsilon_2 = 12 - j\frac{1.0}{w\epsilon_0}$ $\epsilon_3 = 24 - j\frac{2.0}{w\epsilon_0}$ $\epsilon_4 = 5 - j\frac{0.41}{w\epsilon_0}$	$e_1 = 10 - j\frac{0.83}{w\epsilon_0}$ $e_2 = 35 - j\frac{3.0}{w\epsilon_0}$ $e_3 = 5 - j\frac{0.41}{w\epsilon_0}$	Actual and <i>a priori</i> permittivities are different

algorithm when we don't have exact knowledge of the number of permittivities present in the imaging domain. We employed only one *a priori* permittivity (which has the highest value among the 5 used in Case-3) higher than the background value as opposed to Case-3 where 3 *a priori* permittivities were employed higher than the background. This is inspired by the fact that as shown in Fig. 6(a), the highest *a priori* permittivity tends to take part in the reconstruction the most. As shown in Fig. 7, the reconstructed fraction parameters and consequently, the relative permittivity and conductivity of the domain have similar accuracy (even better than Case-3, as shown in Table I). So, we can conclude that, we don't necessarily have to employ the same number of permittivities as *a priori* ones compared to the number of permittivities present in the imaging domain. This will reduce the complexity of the algorithm significantly.

Case-5:

The imaging domain in this case is the same to the one used

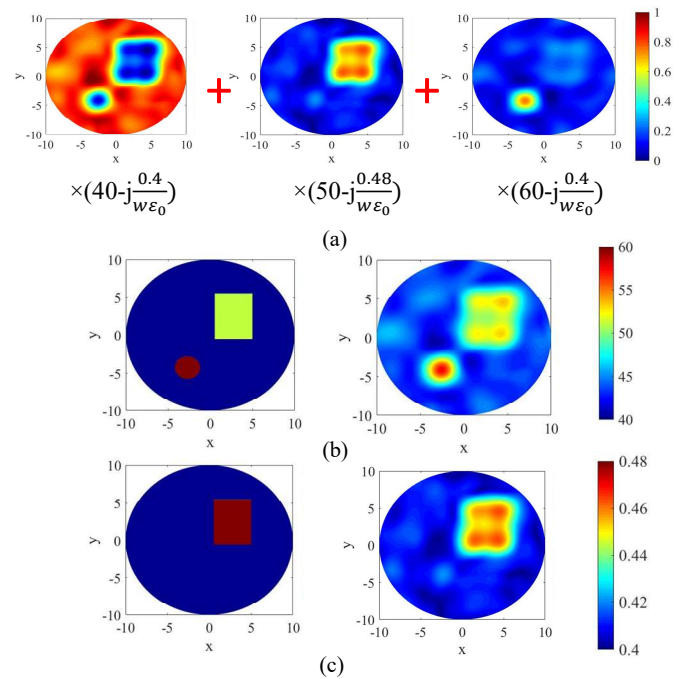


Fig. 5. Reconstructed images (using SNR=20dB) for Case-2: a) images of the three reconstructed fraction parameters, b) corresponding relative permittivity image (right) and actual relative permittivity (left), c) corresponding conductivity image (right) and actual conductivity (left).

in Case-3 and Case-4 except that the circular high permittivity region inside the rectangular region is absent. This represents a case where there is no tumor in the breast. We still use the same set of 3 *a priori* permittivities to assess the robustness of the algorithm in imaging a scenario with or without tumors. As shown in Fig. 8, the reconstructed images are consistent with the actual domain and as expected, both relative permittivity and conductivity are recovered with similar accuracy (Table I). Importantly, it can be deduced from this case that we may assume higher *a priori* permittivity than the highest actual permittivity present in the domain. As reconstructed permittivity (relative permittivity or conductivity) cannot be higher than the assumed maximum *a priori* value, it is safer to assume at least one *a priori* permittivity value high enough so that we don't miss the highest permittivity present in the imaging domain.

In summary, the following points are deduced from the cases shown above: a) the highest (or lowest) *a priori* permittivity/conductivity takes part in the reconstruction process the most, and consequently, b) it is better to keep the number of *a priori* complex permittivities the least to make the algorithm simple, c) the level of the highest (or lowest) *a priori* permittivity/conductivity should be chosen in such a way that the highest (or lowest) permittivity/conductivity of the domain is reconstructed successfully.

IV. SENSITIVITY ANALYSIS

As can be realized, the choice of *a priori* permittivities, e_t may impact the accuracy of the recovered images. It is therefore important to examine any dependence of e_t in the reconstructed images. For this analysis, we consider an

imaging domain where we have one rectangular and one circular anomalies, both having $e_{anom} = 60 - j\frac{0.6}{w\epsilon_0}$ lying in the background of $e_b = 40 - j\frac{0.4}{w\epsilon_0}$, as shown in Fig. 9(a)-10(a). Also, we employ two *a priori* permittivities ($N_{dielec} = 2$) for this sensitivity analysis. The value, $e_1 = 40 - j\frac{0.4}{w\epsilon_0}$ is kept fixed and e_2 is varied. In particular, Figs. 9(b) and 10(b) shows reconstructed images when $e_2 = 70 - j\frac{0.7}{w\epsilon_0}$ and Figs. 9(c), (d) and 10(c), (d) show images for $e_2 = 58 - j\frac{0.7}{w\epsilon_0}$, $46 - j\frac{0.7}{w\epsilon_0}$ and for $e_2 = 70 - j\frac{0.58}{w\epsilon_0}$, $70 - j\frac{0.46}{w\epsilon_0}$, respectively. For Figs. 9(c)-(d), as the selected *a priori* relative permittivities are all lower than the maximum relative permittivity present in the actual domain, the algorithm cannot recover the domain perfectly. Hence, an attempt to reconstruct the relative permittivity (Fig. 9(c)-(d) top) has resulted in an overestimation of the reconstructed conductivity (Fig. 9(c)-(d) bottom). For similar reason, we can see over-estimation of the reconstructed relative permittivity in Figs. 10(c)-(d) top.

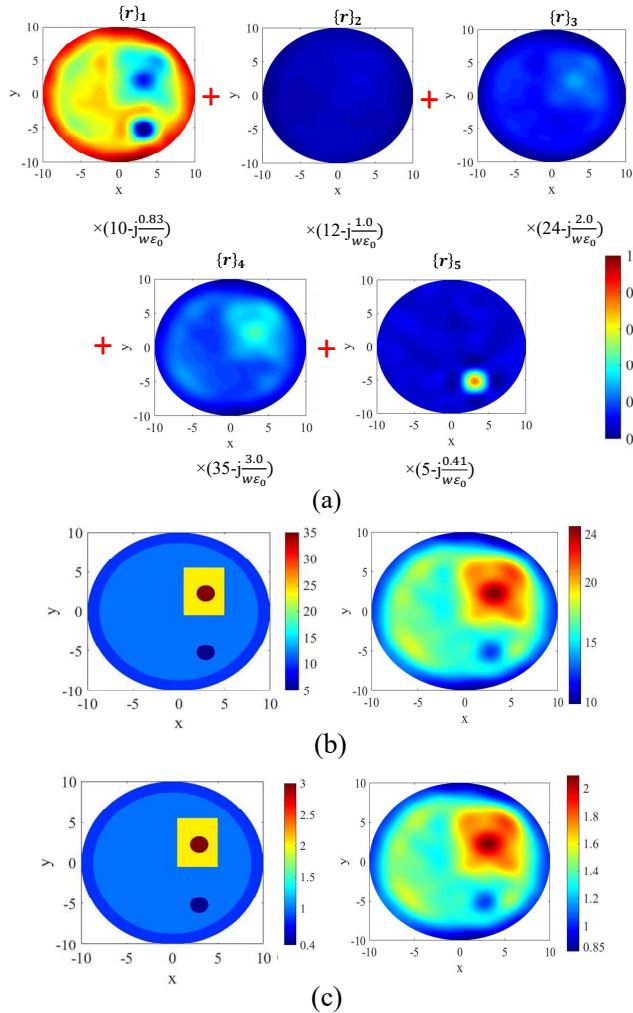


Fig. 6. Reconstructed images (using SNR=20dB) for Case-3: a) images of the five reconstructed fraction parameters, b) corresponding relative permittivity image (right) and actual relative permittivity (left), c) corresponding conductivity image (right) and actual conductivity (left).

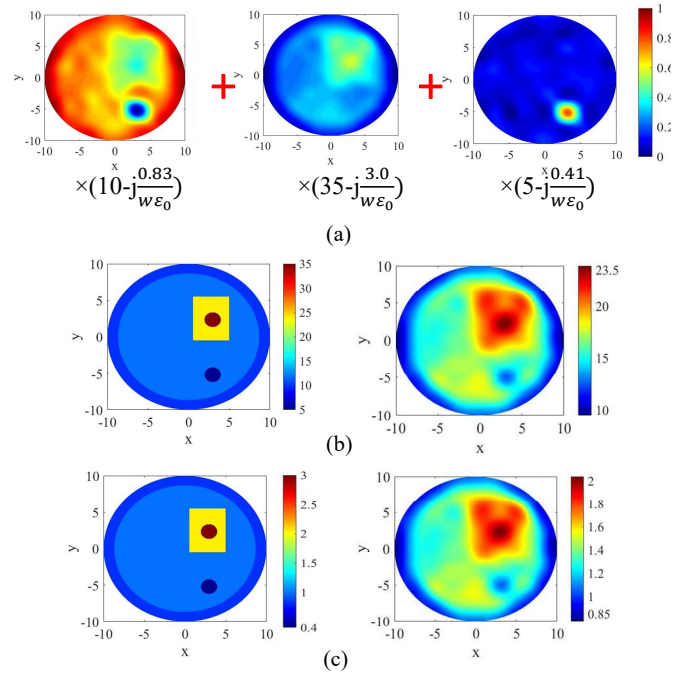


Fig. 7. Reconstructed images (using SNR=20dB) for Case-4: a) images of the three reconstructed fraction parameters, b) corresponding relative permittivity image (right) and actual relative permittivity (left), c) corresponding conductivity image (right) and actual conductivity (left).

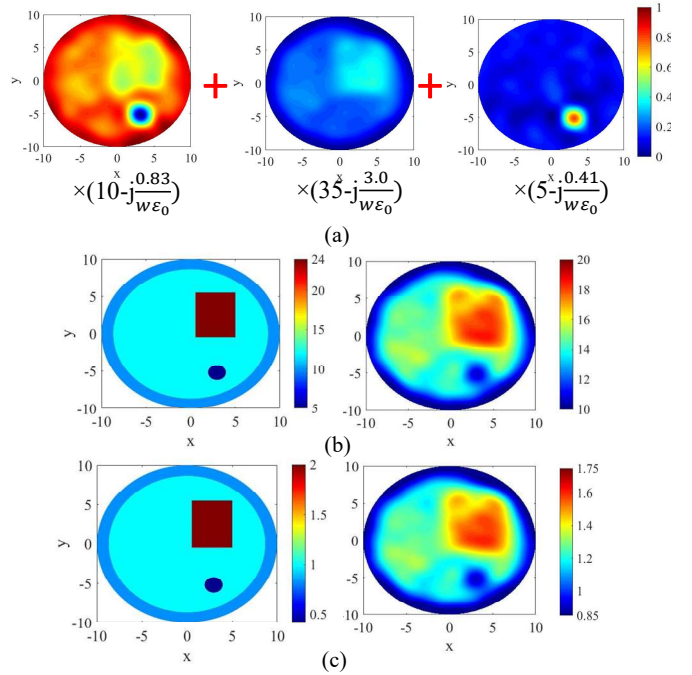


Fig. 8. Reconstructed images (using SNR=20dB) for Case-5: a) images of the three reconstructed fraction parameters, b) corresponding relative permittivity image (right) and actual relative permittivity (left), c) corresponding conductivity image (right) and actual conductivity (left).

Hence, to faithfully recover both the relative permittivity and conductivity, we need to make sure that high enough *a priori* values for both of them are employed in the reconstruction.

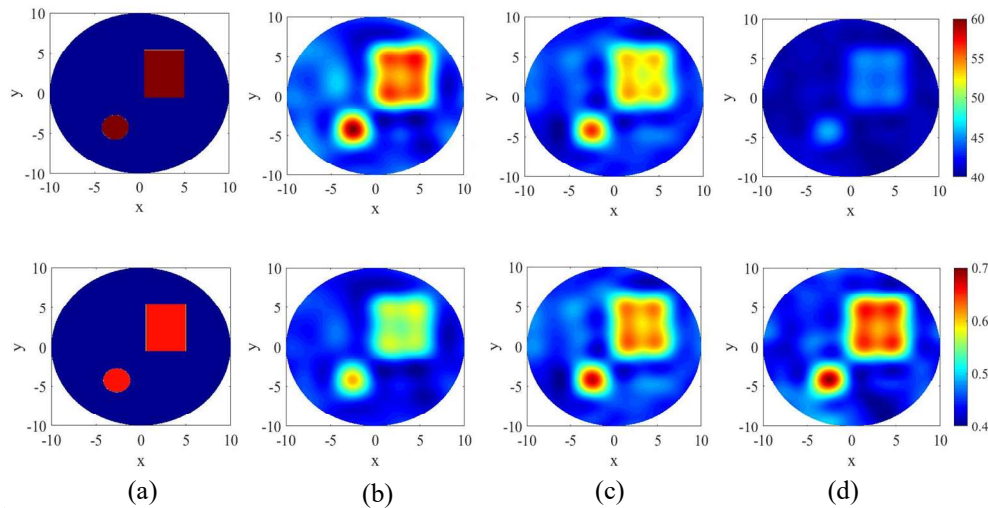


Fig. 9. Sensitivity analysis by varying relative permittivity value of *a priori* permittivity: a) actual imaging domain, b) reconstructed image for $e_1 = 40 - j\frac{0.4}{w\epsilon_0}$ and $e_2 = 70 - j\frac{0.7}{w\epsilon_0}$, c) reconstructed image for $e_1 = 40 - j\frac{0.4}{w\epsilon_0}$ and $e_2 = 58 - j\frac{0.7}{w\epsilon_0}$, d) reconstructed image for $e_1 = 40 - j\frac{0.4}{w\epsilon_0}$ and $e_2 = 46 - j\frac{0.7}{w\epsilon_0}$. Top row: relative permittivity, bottom row: conductivity.

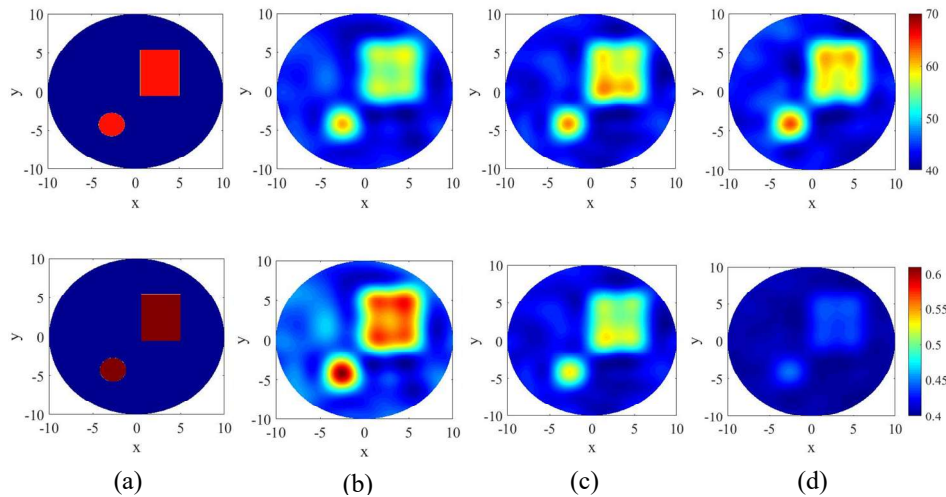


Fig. 10. Sensitivity analysis by varying conductivity value of *a priori* permittivity: a) actual imaging domain, b) reconstructed image for $e_1 = 40 - j\frac{0.4}{w\epsilon_0}$ and $e_2 = 70 - j\frac{0.7}{w\epsilon_0}$, c) reconstructed image for $e_1 = 40 - j\frac{0.4}{w\epsilon_0}$ and $e_2 = 70 - j\frac{0.58}{w\epsilon_0}$, d) reconstructed image for $e_1 = 40 - j\frac{0.4}{w\epsilon_0}$ and $e_2 = 70 - j\frac{0.46}{w\epsilon_0}$. Top row: relative permittivity, bottom row: conductivity.

V. IMAGING RESULTS USING EXPERIMENTAL DATA

A. Experimental Set-up

To validate the proposed imaging method, we employed a glass cylinder of diameter = 20 cm and height=10cm, filled with a biological tissue phantom inside it (see Fig. 11, left side). This cylinder and phantom mimics the set-up employed in Fig. 1(a). As was for the simulations, we used a set of 8 transceiver antennas placed around the cylinder. All dipoles are identical, 6 cm long and matched to 50 Ω . We chose the operating frequency 1.25 GHz with inserted anomalies of diameter, $d = 2.25$ cm. The background medium was prepared following the procedure in [32], viz. by adjusting the ingredients to achieve $\epsilon_r^{back} = 39.8 - j5.4$ (conductivity=0.38 S/m) at 1.25 GHz. The anomaly medium was prepared by

mixing water and glycerin to achieve $\epsilon_r^{anomaly} = 60.2 - j9.1$ (conductivity = 0.63 S/m).

The dielectric permittivity of the materials was measured using the Agilent 85070D dielectric probe kit and *S*-parameter measurements were carried out with a 2-port network analyzer Agilent N5230A. The two ports were connected to the two dipole antennas, one being the transmitter and the other being the receiver. All other dipoles were terminated with 50 Ω loads to minimize reflections.

B. Imaging Results

The images using the measured data are shown in Fig. 11. Again, we observe that the traditional ‘direct’ method leads to pronounced imbalance between the relative permittivity and conductivity images (see Fig. 11(a)). By contrast, the fraction method yields much better balance (for quantitative accuracy, see Table I). Here, Fig. 11(b) is generated by employing

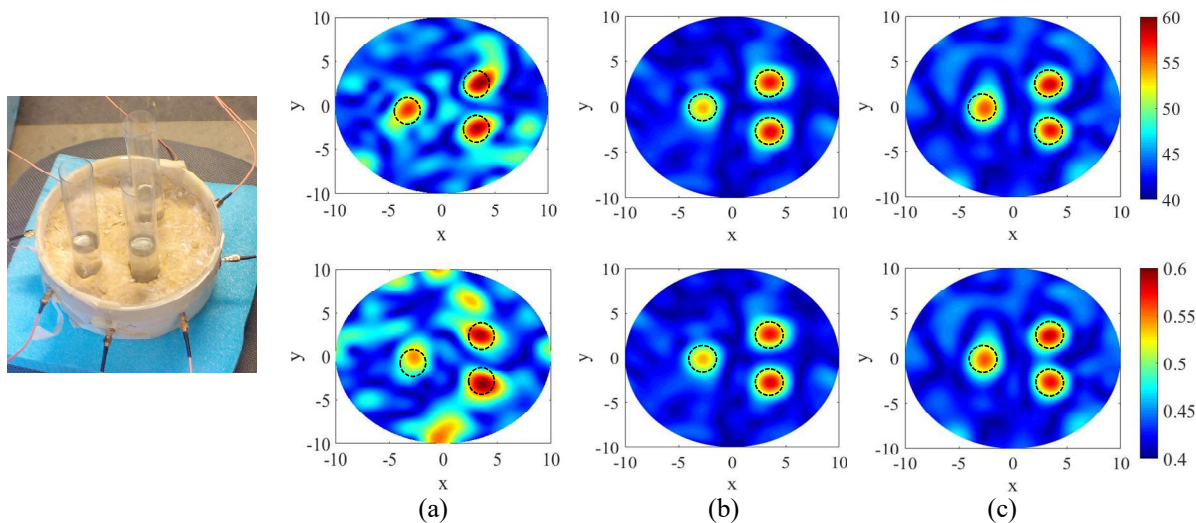


Fig. 11. Reconstructed images using measurement data: (a) direct reconstruction (b) proposed fraction imaging method with $e_1 = 40 - j\frac{0.40}{w\epsilon_0}$ and $e_2 = 60 - j\frac{0.60}{w\epsilon_0}$ (c) proposed fraction imaging method with $e_1 = 40 - j\frac{0.40}{w\epsilon_0}$ and $e_2 = 70 - j\frac{0.70}{w\epsilon_0}$. Top row: relative permittivity, bottom row: conductivity. The dashed circular lines indicate the actual position of the anomaly. The x and y axes are in centimeters. Measurement set-up is shown at the left.

$e_1 = 40 - j\frac{0.40}{w\epsilon_0}$ and $e_2 = 60 - j\frac{0.60}{w\epsilon_0}$ as a priori permittivities. Conversely, Fig. 11(c) is generated by employing $e_1 = 40 - j\frac{0.40}{w\epsilon_0}$ and $e_2 = 70 - j\frac{0.70}{w\epsilon_0}$ as a priori permittivities. The later (Fig. 11(c)) results slightly better image recovery as shown in Table I. As expected, due to model error [27], overall image reconstruction quality is somewhat degraded using the experimental data as compared to that using the synthetic data (see Fig. 4). The slightly lower reconstructed anomaly permittivity and conductivity (see Figs. 11(b), 11(c)) than the expected values are due to the possible measurement error using Agilent 85070D dielectric probe kit while preparing the phantom. Notably, the overall image quality is much better using the proposed method, which is presumably due to the stable nature of the algorithm attributed to the bound check (eqn. (10)).

VI. CONCLUSION

We proposed a new method to improve the accuracy in reconstructing the imaginary part of the complex permittivity using microwave tomography. Specifically, our method corrects the imbalance between the real and imaginary permittivity images. The proposed method is based on constituting the image using a set of *a priori* complex permittivities chosen from the knowledge of the biological domain to be imaged. However, precise knowledge of the domain permittivity is not needed, rather, use of a nominal set of *a priori* values is adequate. The dielectric (relative permittivity and conductivity) is then constructed using a weighted sum (fraction method) of the chosen permittivities. The weights (fractions) are found after applying a standard optimization algorithm, such as, the Gauss-Newton method. To demonstrate the efficacy and robustness of the fraction imaging method, numerous imaging examples involving biological phantoms were used and successful image recovery has been shown. Given that biological media have a strong

imaginary permittivity (conductivity), the proposed method could have a significant impact in the effectiveness of microwave tomography for applications, such as, tumor detection, stroke evolution monitoring etc. among others.

REFERENCES

- [1] Z. Wu et al, "Microwave-tomographic system for oil and gas multiphase flow imaging," *Meas. Sci. and Tech.*, vol. 20, no. 10, May 2009.
- [2] M. Benedetti et al, "An innovative microwave-imaging technique for nondestructive evaluation: applications to civil structures monitoring and biological bodies inspection," *IEEE Trans. Instrum. Meas.*, vol. 55, no. 6, pp. 1878–1884, Dec. 2006.
- [3] L. M. Neira et al, "High-resolution microwave breast imaging using a 3-d inverse scattering algorithm with a variable-strength spatial prior constraint," *IEEE Trans. Ant. & Prop.*, vol. 65, no. 11, pp. 6002–6014, 2017.
- [4] M. Haynes et al, "Real-time microwave imaging of differential temperature for thermal therapy monitoring," *IEEE Trans. Biomed. Engg.*, vol. 61, no. 6, pp. 1787–1797, 2014.
- [5] G. Chen et al, "Real-time 3d microwave monitoring of interstitial thermal therapy," *IEEE Trans. Biomed. Engg.*, vol. 65, no. 3, pp. 528–538, 2018.
- [6] J. M. Geffrin et al, "3-D imaging of a microwave absorber sample from microwave scattered field measurements," *IEEE Micro. & Wireless Comp. Lett.*, vol. 25, no. 7, pp. 472–474, 2015.
- [7] M. A. Islam et al, "A novel method of deep tissue biomedical imaging using a wearable sensor," *IEEE Sensors Journal*, vol. 16, no. 1, pp. 265–270, 2016.
- [8] M. A. Islam et al, "A modified Gauss-Newton algorithm for fast microwave imaging using near-field probes," *Microwave and Optical Tech. Letters*, vol. 59, no. 6, pp. 1394–1400, 2017.
- [9] Z. Liu et al, "Subspace-based variational Born iterative method for solving inverse scattering problems," *IEEE Geosci. Remote Sens. Lett.*, vol. 16, no. 7, pp. 1017–1020, July 2019.
- [10] T. J. Cui and W. C. Chew, "Inverse scattering of two-dimensional dielectric objects buried in a lossy earth using the distorted born iterative method," *IEEE Trans. Geosci. Remote Sens.*, vol. 39, no. 2, pp. 339–346, Feb. 2001.
- [11] T. Rekanos and A. Raisanen, "Microwave imaging in the time domain of buried multiple scatterers by using an FDTD-based optimization technique," *IEEE Trans. Magn.*, vol. 39, no. 3, pp. 1381–1384, May 2003.

- [12] D. Liet et al, "Conformal microwave imaging for breast cancer detection," *IEEE Trans. Microw. Theory Tech.*, vol. 51, no. 4, pp. 1179–1186, Apr. 2003.
- [13] T. Takenaka et al, "Inverse scattering for a three dimensional object in the time domain," *J. Opt. Soc. Amer.: A*, vol. 20, no. 10, pp. 1867–1874, 2003.
- [14] Z. Q. Zhang and Q. H. Liu, "Three-dimensional nonlinear image reconstruction for microwave biomedical imaging," *IEEE Trans. Biomed. Eng.*, vol. 51, no. 3, pp. 544–548, Mar. 2004.
- [15] A. E. Bulyshev et al, "Three-dimensional vector microwave tomography: Theory and computational experiments," *Inverse Problems*, vol. 20, pp. 1239–1259, 2004.
- [16] T. Rubaek et al, "Nonlinear microwave imaging for breast-cancer screening using Gauss–Newton's method and the CGLS inversion algorithm," *IEEE Trans. on Ant. & Prop.*, vol. 55, no. 8, pp. 2320–2330, 2007.
- [17] P. M. Meaney et al, "Pre-scaled two-parameter Gauss-Newton image reconstruction to reduce property recovery imbalance," *Phys. Med. Biol.*, vol. 47, pp. 1101–1119, 2002.
- [18] M. Zhang and M. Soleimani, "Simultaneous reconstruction of permittivity and conductivity using multi-frequency admittance measurement in electrical capacitance tomography," *Meas. Sci. and Tech.*, vol. 47, pp. 025405–025417, 2016.
- [19] N. K. Nikolova, "Microwave imaging for breast cancer," *IEEE Microw. Mag.*, vol. 12, no. 7, pp. 78–94, Dec. 2011.
- [20] D. W. Winterset et al, "Three-dimensional microwave breast imaging: dispersive dielectric properties estimation using patient-specific basis function," *IEEE Trans. Med. Imag.*, vol. 28, no. 7, pp. 969–981, 2009.
- [21] M. Ostadrahimi et al, "A near-field dual polarized (TE–TM) microwave imaging system," *IEEE Trans. on Micro. Theory & Tech.*, vol. 61, no. 3, pp. 1376–1384, 2013.
- [22] C. Gilmore et al, "A wideband microwave tomography system with a novel frequency selection procedure," *IEEE Trans. Biomed. Engg.*, vol. 57, no. 4, pp. 894–904, 2010.
- [23] N. R. Epstein et al, "Microwave tomographic imaging utilizing low-profile, rotating, right angle-bent monopole antennas," *Int. Journal of Antennas & Prop.*, <http://dx.doi.org/10.1155/2014/431602>, 2014.
- [24] E. Malone et al, "Stroke type differentiation using spectrally constrained multifrequency EIT: evaluation of feasibility in a realistic head model," *Phys. Meas.*, vol. 35, pp. 1051–1066, 2014.
- [25] O. Crabeck et al., "Imaging air volume fraction in sea ice using non-destructive X-ray tomography," *The Cryosphere*, vol. 10, pp. 1125–1145, 2016.
- [26] M. A. Islam et al, "A microwave tomographic technique to enhance real-imaginary permittivity image quality," *Proceedings of the IEEE Int. Symp. Antennas and Propagation (APS/URSI)*, San Diego, CA, USA, July, 2017.
- [27] J. Nocedal and S. Wright, *Numerical optimization*, 2nd ed. Springer: LLC, 2006.
- [28] P. C. Hansen, *Discrete inverse problems: numerical aspects of linear inversion*, SIAM series on Fundamentals of Algorithms, 2010.
- [29] S. Gabriel et al, "The dielectric properties of biological tissues—Part II: Measurement in the frequency range 10 Hz to 20 GHz," *Phys. Med. Biol.*, vol. 41, pp. 2251–2269, 1996.
- [30] S. Gabriel et al, "The dielectric properties of biological tissues: III. Parametric models for the dielectric spectrum of tissues," *Phys. Med. Biol.*, vol. 41, pp. 2271–2293, 1996.
- [31] A. Afsari et al., "A rapid medical microwave tomography based on partial differential equations," *IEEE Trans. on Ant. & Prop.*, vol. 66, no. 10, pp. 5521–5535, 2018.
- [32] K. F. Ito et al, "Development and characteristics of a biological tissue-equivalent phantom for microwaves." *Electronics and Communications in Japan (Part I: Communications)*, vol. 84, pp. 67–77, 2001.